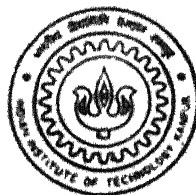


Simulation and Correction of the Beam Hardening effect in X-ray Tomography

by

K. Rama Krishna

TH
NET/2000/1M
K 897.3



NUCLEAR ENGINEERING AND TECHNOLOGY PROGRAMME
INDIAN INSTITUTE OF TECHNOLOGY KANPUR

April, 2000

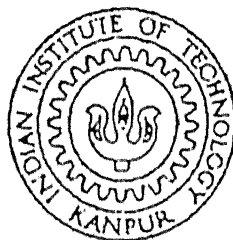
*Simulation and Correction of the Beam Hardening effect
in X- ray Tomography*

*A Thesis Submitted
in Partial Fulfillment of the Requirements
for the Degree of*

Master of Technology

by

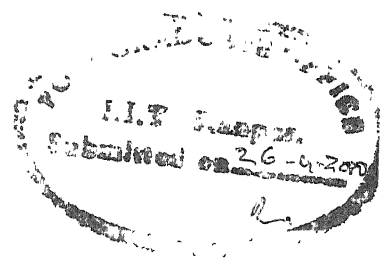
K. Rama Krishna



Nuclear Engineering and Technology Programme

Indian Institute of Technology, Kanpur

April 2000



Certificate

It is certified that work contained in the thesis entitled, *Simulation and correction of the Beam Hardening effect in X - ray tomography*, by K. Rama Krishna, has been carried out under our supervision and this work has not been submitted elsewhere for a degree.

A handwritten signature in black ink, appearing to read "Prabhat Munshi".

Dr. Prabhat Munshi,
Professor,
Department of Mechanical
Engineering,
Indian Institute of Technology,
Kanpur 208 016.

A handwritten signature in black ink, appearing to read "M. S. Kalra".

Dr. M. S. Kalra,
Professor,
Department of Mechanical
Engineering,
Indian Institute of Technology,
Kanpur 208 016.

April, 2000.

Acknowledgements

I would like to express my deep felt sincere gratitude and appreciation to my thesis supervisors Dr. P. Munshi and Dr. M. S. Kalra for their skillful guidance, constant supervision, timely suggestions in carrying out the present work.

I owe my sincere thanks to Dr. K. Muralidhar for his tireless supervision, encouragement and moral support throughout the course of this work.

I acknowledge my heartiest regards and reverence to my beloved parents for their deep affection and moral support.

I would like to thank my friends Sunect, Farhan, Sharad and Ruchi for helping me and providing a homely atmosphere. Their company made my stay at iitk memorable.

Abstract

Polychromatic X-ray sources are universally used in computerized tomography to obtain adequate intensity. These sources, however, can produce some artifacts in the reconstructed image due to non-linearities. Beam hardening is one such artifact, which produces false line integrals.

The present investigation involves how one can estimate from the total attenuation, p , of a polyenergetic X-ray beam what the total attenuation, m , of a monoenergetic beam would have been along the same ray. In the present work three different specimens are studied which have different geometries. Simulation results show the introduction of beam hardening although the projection data are qualitatively same but quantitatively different.

The polynomial approximation method is working well. For a typical X-ray spectra passing through the material one can find a simple function f such that $f(p)$ is a sufficiently close estimate of m to allow good reconstructions.

Contents

<i>List of tables</i>	i
<i>List of figures</i>	iii
1 Introduction	1
1.1 An overview of computerized tomography	1
1.2 Image Reconstruction from projections	4
1.3 An overview of present work	5
1.3.1 The problem of Beam Hardening.....	5
1.4 Thesis layout	8
2 Theoretical Formulation	9
2.1 Preliminaries	9
2.2 Data collection Mode	10
2.3 CBP Algorithm	12
2.4 Formula for polyenergetic radiation	14
2.5 Displaying of an image	18
2.5.1 VIBGYOR Representation of CT Images.....	19

3	Simulation of beam hardening effect	21
3.1	Simulation of polyenergetic projection data.....	21
4	Correction of beam hardening effect	28
4.1	Correction method for beam hardening	28
5	Results and Discussions	40
5.1	Error measurements	40
5.2	Simulation results	47
5	Conclusions	48
	References	49

List of Tables

3.1	X- ray spectrum for S1	22
3.2	X- ray spectrum for S2	24
3.3	X- ray spectrum for S3	26
5.1	Average pixels errors between the projection data for S1	41
5.2	Root mean square errors between the projection data for S1	41
5.3	Average pixel errors between the original and various reconstructed data for S1	42
5.4	Root mean square errors between the original and various reconstructed data for S1	42
5.5	Average pixels errors between the projection data for S2	43
5.6	Root mean square errors between the projection data for S2	43
5.7	Average pixel errors between the original and various reconstructed data for S2	44
5.8	Root mean square errors between the original and various reconstructed data for S2	44

5.9 Average pixels errors between the projection data for S3 45

5.10 Root mean square errors between the projection data for S3 45

5.11 Average pixel errors between the original and
various reconstructed data for S3 46

5.12 Root mean square errors between the original and
various reconstructed data for S3 46

List of Figures

1.1	Different material attenuate the X- ray differently	1
1.2	A Radon value is the line integral along the line L	2
1.3	The Fourier slice theorem	3
1.4	Computing the inverse of the Radon transform	4
1.5	Outline of the mathematical and computational procedure in CT	7
2.1	Data collection geometry	11
2.2	Derivation of polychromatic ray sum	15
3.1	Original image of S1 at energy 60 keV	23
3.2	Beam hardening reconstructed image of S1	23
3.3	Original image of S2 at energy 0.3 MeV	25
3.4	Beam hardening reconstructed image of S2	25
3.5	Original image of S3 at energy 60 keV	27
3.6	Beam hardening reconstructed image of S3	27
4.1	Flow chart representing the correction procedure.....	32
4.2	First reconstructed image of S1 at energy 60 keV	33

4.3	Second reconstructed image of S1 at energy 60 keV	33
4.4	Third reconstructed image of S1 at energy 60 keV	34
4.5	Monochromatic reconstructed image of S1 at energy 60 keV	34
4.6	First reconstructed image of S2 at energy 0.3 MeV	36
4.7	Third reconstructed image of S2 at energy 0.3 MeV	36
4.8	Monochromatic reconstructed image of S2 at energy 0.3 MeV	37
4.9	First reconstructed image of S3 at energy 60 keV	38
4.10	Second reconstructed image of S3 at energy 60 keV	38
4.11	Monochromatic reconstructed image of S3 at energy 60 keV	39

Chapter 1

Introduction

The technique of computerized tomography(CT) has established itself as a leading tool in diagnostic radiology over the past thirty years and is catching on fast in the nondestructive evaluation area in a variety of situations. The first CT scanner was developed by Hounsfield (1973) who was later on awarded the Nobel prize for medicine. In past, CT was done by X-rays but now other sources like γ -ray, laser, ultrasonic resonance etc. are also used. There has been a very great deal of activity in recent years to find algorithms which are fast when implemented on a computer and which produce acceptable reconstructions in spite of the finite and inaccurate nature of the data.

1.1 An Overview of computerized tomography

The aim of computerized tomography is to assign to every point inside the object a number, which is specific to the material occupying that point. A suitable candidate for this number is the X- ray attenuation coefficient of the material.

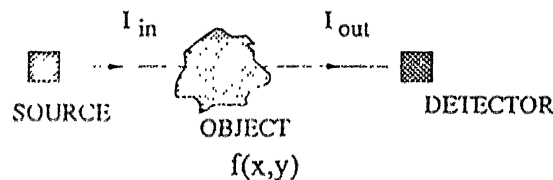


Fig. 1.1 Different materials attenuate the X- ray differently.

Introduction

The object function is denoted by $f(x, y)$. The relation between the intensities I_{in} and I_{out} in Fig. 1.1 is described by

$$I_{out} = I_{in} \exp\left(-\int_L f(x, y) dl\right) \quad (1.1)$$

By taking the natural logarithm we get

$$\ln\left[\frac{I_{in}}{I_{out}}\right] = \int_L f(x, y) dl \quad (1.2)$$

This means that what we read in detector is the line integral of the object function. This object function $f(x, y)$, for X-ray / γ -ray setup, represents the linear attenuation coefficient, $\mu(x, y)$, characteristic of the material.

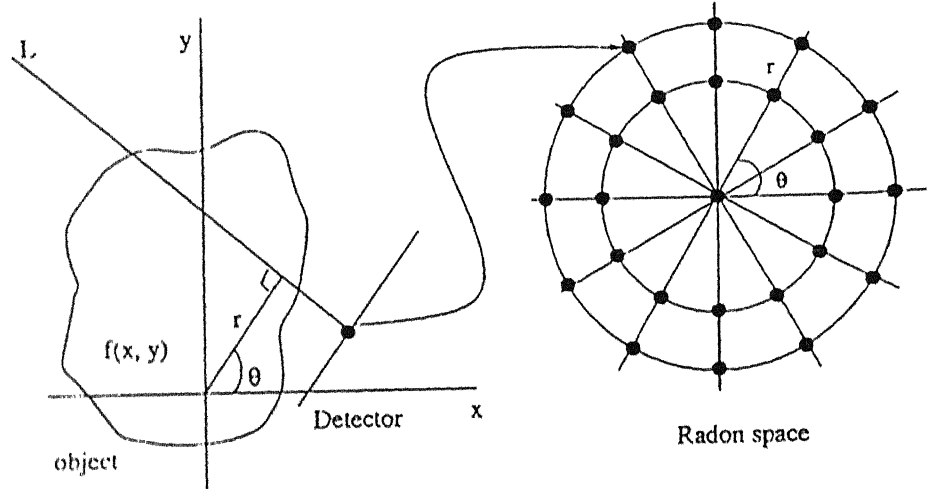


Fig. 1.2 A Radon value is the line integral along the line L.

The radon transform $R[f(r, \theta)]$, or the projection $p(r, \theta)$, of an object $f(x, y)$ is the line integrals through the object in all possible directions. This means, a single Radon value is the integral of all points along a line with angle and perpendicular

Introduction

distance r from the origin (Fig 1.2). The Radon transform (Herman 1980) can be written as

$$p(r, \theta) = R [f(r, \theta)] = \iint f(x, y) \delta(x \cos \theta + y \sin \theta - r) dx dy \quad (1.3)$$

An important relationship between the Radon transform and the Fourier transform is the Fourier slice theorem. The theorem states that the one dimensional Fourier transform of the Radon transform along a radial line is identical to the same line in the

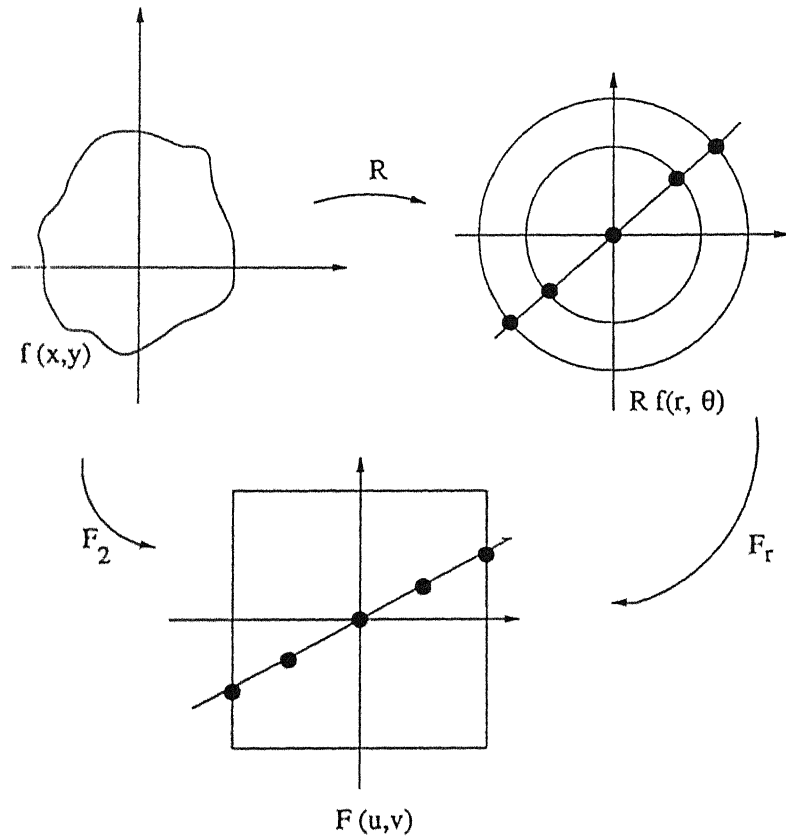


Fig. 1.3 The Fourier slice theorem.

Introduction

two dimensional Fourier transform of the object.

$$F [R [f(R, \theta)]] = F_2 [R [f(R \cos \theta, R \sin \theta)]] \quad (1.4)$$

The theorem is illustrated in Fig. 1.3 .

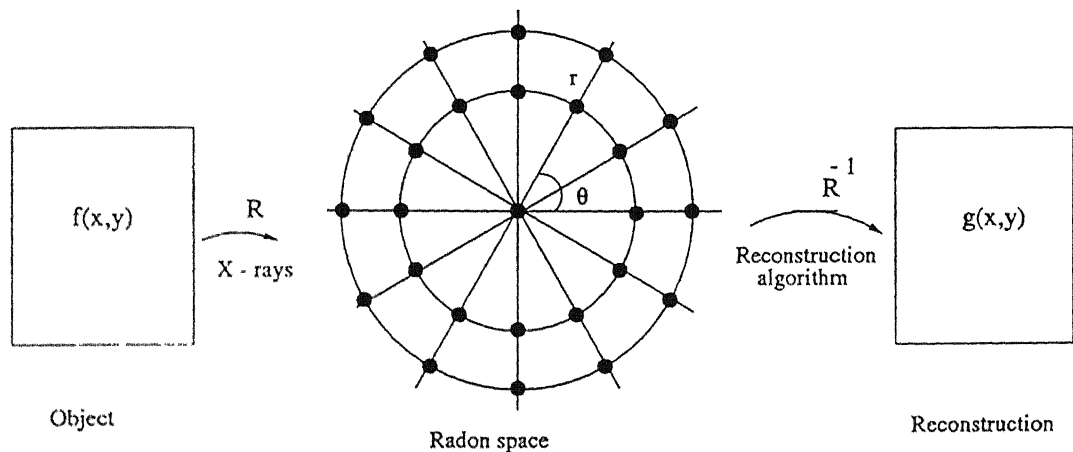


Fig. 1.4 Computing the inverse of the Radon transform.

1.2 Image Reconstruction from projections

The range of applicability of image reconstruction is very wide. At one end, data from electron microscope are used to reconstruct the molecular structure of bacteriophages, while at the other end data collected by the rockets sent outside the earth's atmosphere are used to reconstruct the X-ray structure of the supernova remnants. Image reconstruction can very aptly defined in words of Herman (1980) as :

“ Image reconstruction from projections is the process of producing an image of a two dimensional distribution (usually of some physical property) from estimates of its line integrals along a finite number of lines of known locations”.

1.3 An overview of the present work

The measurements in computed tomography can only be used to estimate the line integrals. Inaccuracies in these estimates are due to the width of the X-ray beam, hardening of the beam, photon statistics, etc. Radon's inverse formula is sensitive to these inaccuracies.

When an X-ray beam passes through the material, its attenuation at any point depends on the material at that point and on the energy distribution (spectrum) of the beam. A difficulty arises due to the fact that the X-ray beam used in computed tomography consists of photons at different energies. The attenuation at a fixed point is generally greater for photons of lower energy as a result the energy distribution (spectrum) of the X-ray beam changes (hardens) as it passes through the material. X-ray beam reaching a particular point inside the material from different directions are likely to have different spectra (having passed through different materials before reaching the point of interest) and thus will be attenuated differently at that point. This makes it difficult to assign a single value for the attenuation coefficient at that point inside the material.

1.3.1 The problem of Beam Hardening

The aim of computed tomography is to obtain information regarding the nature of material occupying exact positions inside the object.

In computed tomography we have two sets of measurements:

(i) Calibration measurements, on which we can base an estimate of what the detector measurements would be if the object to be reconstructed is not between the source and the detector .

Introduction

(ii) Actual detector measurements with the object of interest in position.

The method by which these measurements are taken is shown in Fig.1.5. There is a region of space (referred to as reconstruction region in Fig. 1.5) is occupied by some homogeneous reference material such as air or water during the calibration measurement. During the actual measurement, the object of interest is inserted into the reconstruction region, (partially) replacing the reference material. It is an important restriction that the object of interest does not occupy any point outside the reconstruction region.

Suppose that we have a monoenergetic X-ray source with photon energy \bar{e} . For a fixed source and detector pair, let C_m be the calibration measurement, and let A_m be the actual measurement. We can define monochromatic ray sum, m , for this beam by

$$m = - \ln \left(\frac{A_m}{C_m} \right) \quad (1.5)$$

and we refer to the set of m 's for all source and detector pair positions as the monochromatic projection data. In practice, the X-ray beam is polychromatic. Let C_p and A_p denote calibration and the actual measurement, respectively. We can define polychromatic ray sum, p , for this beam by

$$p = - \ln \left(\frac{A_p}{C_p} \right) \quad (1.6)$$

and we refer to the set p 's for all source-detector pair positions as the polychromatic projection data.

The problem of beam hardening is that for any source and detector pair we can obtain p , but reconstruction procedure requires m as per Eq. (1.5). Beam hardening results in false gradients of the linear attenuation coefficients in the CT cross section images, indicating a non-existent density or composition gradient in the imaged object. Correction for beam hardening effect is a must in Quantitative Computerized Tomography (QCT). For a given total attenuation of polyenergetic X-ray beams

Introduction

through the object, one has to estimate the total attenuation of monoenergetic X – ray beams through the same parts of the object which are precise enough for useful reconstruction of the monoenergetic linear attenuation coefficients in the material object. The mathematical and computational procedures in CT imaging are summarized in Fig. 1.5.

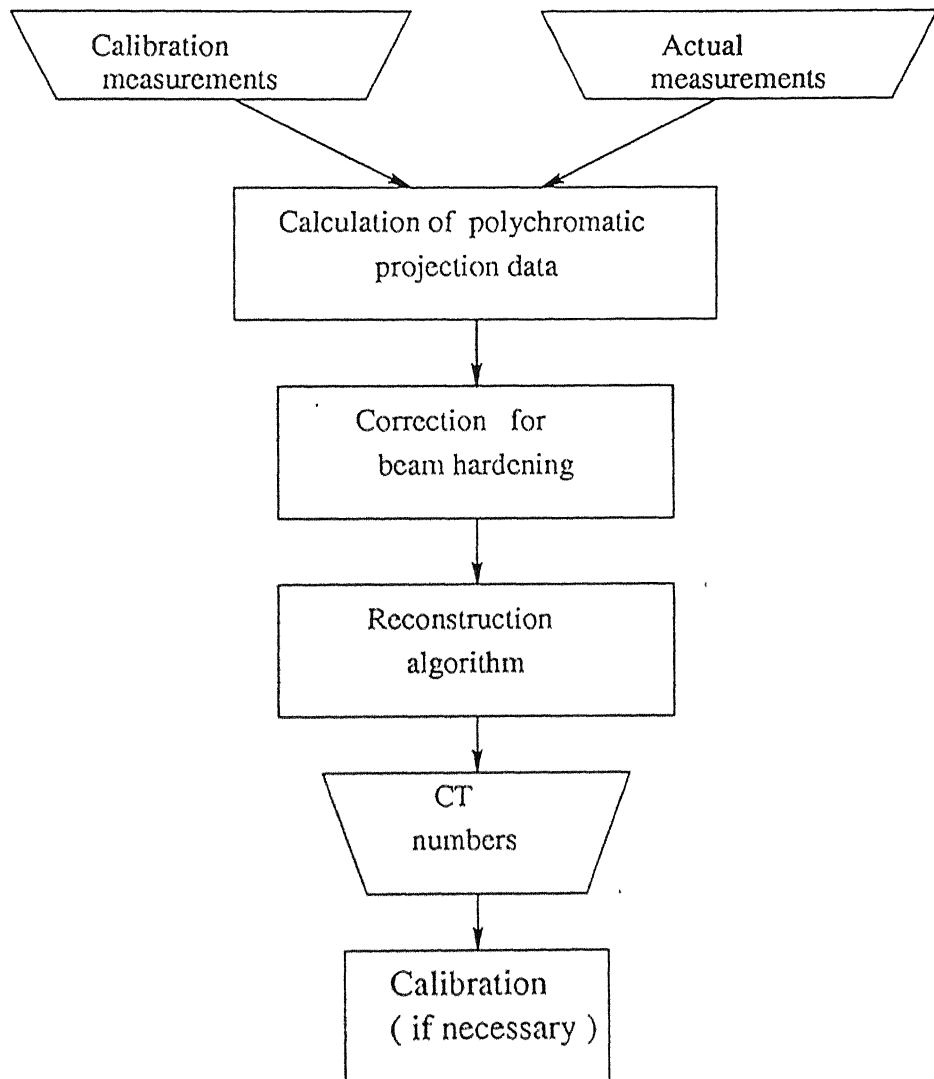


Fig. 1.5 Outline of the mathematical and computational procedures in CT.

1.4 Thesis layout

- *Chapter 2* gives the detail of the reconstruction algorithm (CBP) and derivation of formulae for polyenergetic radiation.
- *Chapter 3* gives the details of the simulation beam hardening effect of the specimens.
- *Chapter 4* gives the details of the method for removing the beam hardening effect in computerized tomography.
- *Chapter 5* provides discussions on the results based on the simulated data.
- *Chapter 6* summarizes the conclusions and suggests scope for further work.

Chapter 2

Theoretical Formulation

In this section, the computational and mathematical procedures underlying the data collection, image reconstruction, formula for polyenergetic radiation and image display used in the CT are discussed.

2.1 Preliminaries

The number of counts of photon after passing through a curve 'c' in the material being tested is given by

$$N = N_0 \exp(-\int_c \mu(r, \phi) dl) \quad (2.1)$$

where the integration is along the chord length of 'c',

N is the number of photon counts after traversing the chord length,

N_0 is the initial photon counts and

Theoretical formulation

μ is the attenuation coefficient. Since μ depends on the material and the energy of the radiation, a distribution of μ is a direct indicator of the material composition of the component being studied.

Equation 2.1 can be written as

$$\ln\left(\frac{N}{N_0}\right) = \int_c \mu(r, \phi) dl = p(s, \theta) \quad (2.2)$$

where $p(s, \theta)$ is called the projection data for the tomographic algorithm, and it is the integral of the function along the line specified by S and θ (Fig. 2.1).

The aim of tomography is to reconstruct the function $\mu(r, \phi)$, if a set of several p -values ($p(s, \theta)$) measured along various chords (c) is given. This is the fundamental problem of CT and CBP has been used in the present study for that purpose. The μ values can be suitably normalized to get the material density distribution, if so desired.

2.2 Data Collection Mode

The image processing methodology requires attenuation data to be collected by an array of radiation detectors for the reconstruction of the function $\mu(r, \phi)$. In this study the mode of collection is the Parallel Beam Geometry (PBG) mode (Fig. 2.1). This system consists of several pairs of radiation source and radiation detector, which can scan the object completely. The SD (source detector) pairs are spaced uniformly and the object can be rotated to get the data for different views. The line SD represents the path of the data ray or the chord along which the function $p(s, \theta)$ can be found out. The

Theoretical formulation

perpendicular distance from the center of the object to the path of the ray is denoted by S . The object table is rotated to get several sets of ' p ' for different values of θ .

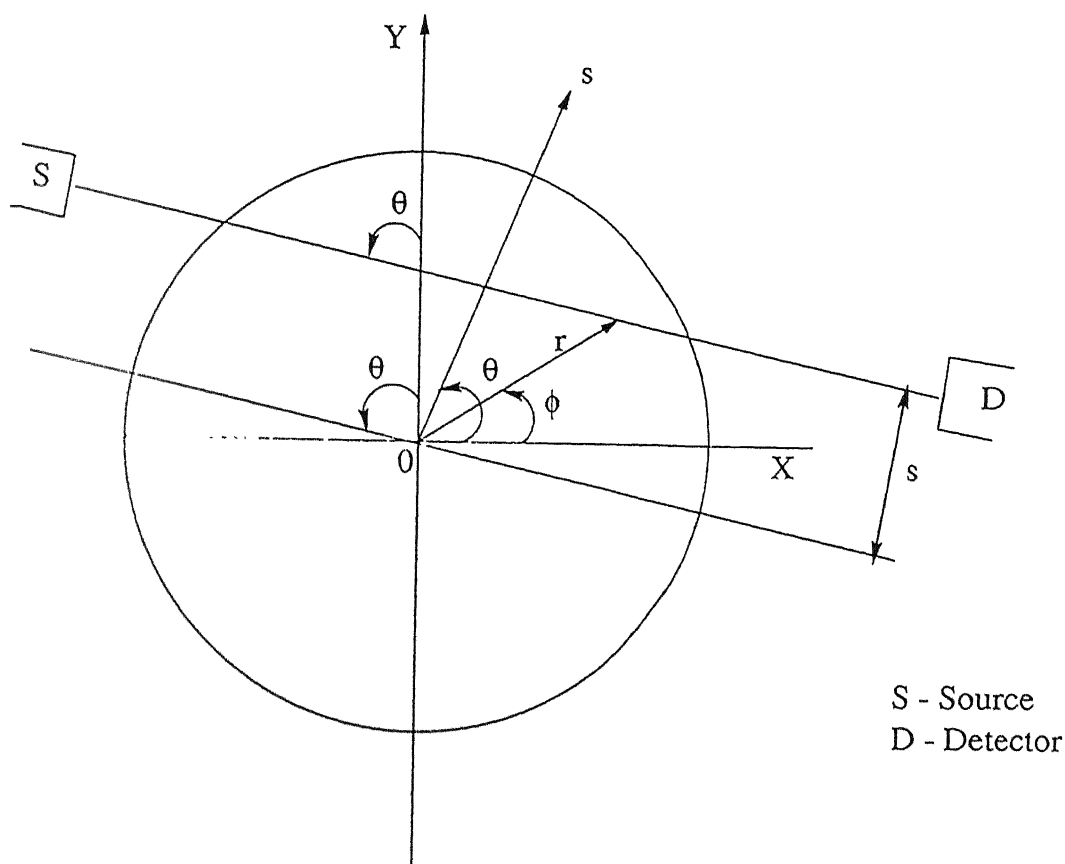


Fig. 2.1 Data collection geometry.

Typical values of the number of rays and the number of projections used in the present work are 100 and 100. The source-detector system is moved pixel by pixel, thus generating a grid of 100 by 100 over the physical region of interest.

2.3 CBP Algorithm

Convolution Backprojection (CBP) algorithm has been described in great detail by Herman (1980). In this section we review CBP briefly as reported earlier by Munshi (1992).

Fig. 2.1 shows the data collection geometry for a parallel beam CT scanner. The object function, $\mu(r, \phi)$, denoted for generality by $f(r, \phi)$ in subsequent equations, is represented by a unit circle and one (of many) data rays is represented by SD. The ray indices are S and θ , where S is the perpendicular distance of the ray from the object center, and θ is the angle of the source position (or object rotation). The CT data denoted by $p(s, \theta)$ given by

$$p(s, \theta) = \int_{SD} f(r, \phi) dz \quad (2.3)$$

Here, Z is the variable of integration along the chord SD. The CT machine collects the projection data $p(s, \theta)$ for many values of S and θ . The “projection slice theorem” Herman(1980) states the equivalence of the two-dimensional Fourier transform of $f(r, \phi)$ and the 1-dimensional Fourier transform of $p(s, \theta)$ with respect to S . Symbolically

$$\hat{p}(R, \theta) = \hat{f}(R \cos \theta, R \sin \theta) \quad (2.4)$$

where the symbol \wedge represents the Fourier transform and R is the spatial Fourier frequency. A two-dimensional Fourier inversion of Equation 2.4 leads to the well-known tomographic inversion formula

$$f(r, \phi) = \int_{0-\infty}^{\pi \infty} \int \hat{p}(R, \theta) e^{i2\pi Rr \cos(\theta-\phi)} |R| dR d\theta \quad (2.5)$$

where

Theoretical formulation

$$\hat{p}(R, \theta) = \int_{-\infty}^{\infty} \hat{p}(s, \theta) e^{-i2\pi R s} ds \quad (2.6)$$

We note that the inner integral in Equation 2.5 is divergent. A practical implementation of Equation 2.5 incorporates the replacement of the factor $|R|$ by $|R|W(R)$. Where $W(R)$ is a suitable window function that vanishes outside the interval $[R_c, R_c]$. Here, $|R_c|$ is the Fourier cutoff frequency. Normally, $W(R)$ is an even function of R . Thus Equation 2.5 takes the approximate form

$$\tilde{f}(r, \phi) \approx \int_{0-\infty}^{\pi \infty} \int \hat{p}(R, \theta) e^{i2\pi R r \cos(\theta - \phi)} |R| W(R) dR d\theta \quad (2.7)$$

If $\hat{p}(R, \theta)$ also vanishes for $|R| \geq R_c$, then the reconstructed function, denoted by \tilde{f} , agrees exactly with $f(r, \phi)$ with the following window function

$$\begin{aligned} W(R) &= 1, & |R| \leq R_c \\ &= 0, & |R| > R_c \end{aligned} \quad (2.8)$$

Equation 2.8 and the convolution theorem of Fourier transforms give the reconstructed function \tilde{f} as

$$\tilde{f}(r, \phi) = \int_{0-\infty}^{\pi \infty} \int p(s, \theta) q(s' - s) ds d\theta \quad (2.9)$$

where

$$q(s) = \int_{-\infty}^{\infty} |R| W(R) e^{i2\pi R s} dR \quad (2.10)$$

and

$$s' = r \cos(\theta - \phi). \quad (2.11)$$

Theoretical formulation

The index s' is the data ray passing through (r, ϕ) , the point being reconstructed. The inner integral in the Equation 2.9 is a one-dimensional convolution and the outer integral, corresponding to the averaging operation (over θ), is termed as backprojection and hence the name convolution backprojection for this particular implementation. The CBP method is also known as the filtered backprojection algorithm because of the “filtering” of the Fourier transform of the projection data \hat{p} by the window (or filter) $W(R)$ in the initial stages of the formulation given by Equation 2.5. The function $q(s)$, known as the convolving function, is evaluated once and stored for the repeated use for different views (or different angles θ).

For a given point (r, ϕ) , the inherent error E_1 , in the CBP implementation, Equation 2.9 is,

$$E_1(r, \phi) = f(r, \phi) - \tilde{f}(r, \phi) \quad (2.12)$$

where f and \tilde{f} are given by Equation 2.5 and Equation 2.9 respectively. This error is strictly due to finite cut-off, R_c of the Fourier frequency and is precisely zero if the projection data happens to be band-limited and the cut-off frequency is chosen to be the highest frequency contained in \hat{p} . In general, to avoid aliasing artifacts Herman (1980) has recommended the choice, $R_c = 1/(2\Delta s)$, where Δs is the spacing of the data rays.

2.4 Formula for polyenergetic radiation

The linear X-ray attenuation coefficient at a point inside a cross section of the object depends on the position of the point (x, y) and on the X-ray energy e . It can be denoted as $\mu(x, y, e)$. From equation 2.2 in case of monochromatic beam it can be written as

Theoretical formulation

$$m_L = \int_L \mu(x, y, e) dl. \quad (2.12)$$

In case of polychromatic beam the result will not be m_L , but rather an estimate for the more complicated integral

$$p_L = -\ln \int_0^\infty \tau(e) \exp\left(-\int_L \mu(x, y, e) de\right) de. \quad (2.13)$$

Where $\tau(e)$ is the probability that the detected photon is at energy e .

It is derived in the following manner (Herman (1979)):

Let $\mu_e(z)$ denote the linear attenuation coefficient at energy e at the point Z between the source ($Z = Z_s \leq 0$) and the detector ($Z = Z_d = D$).

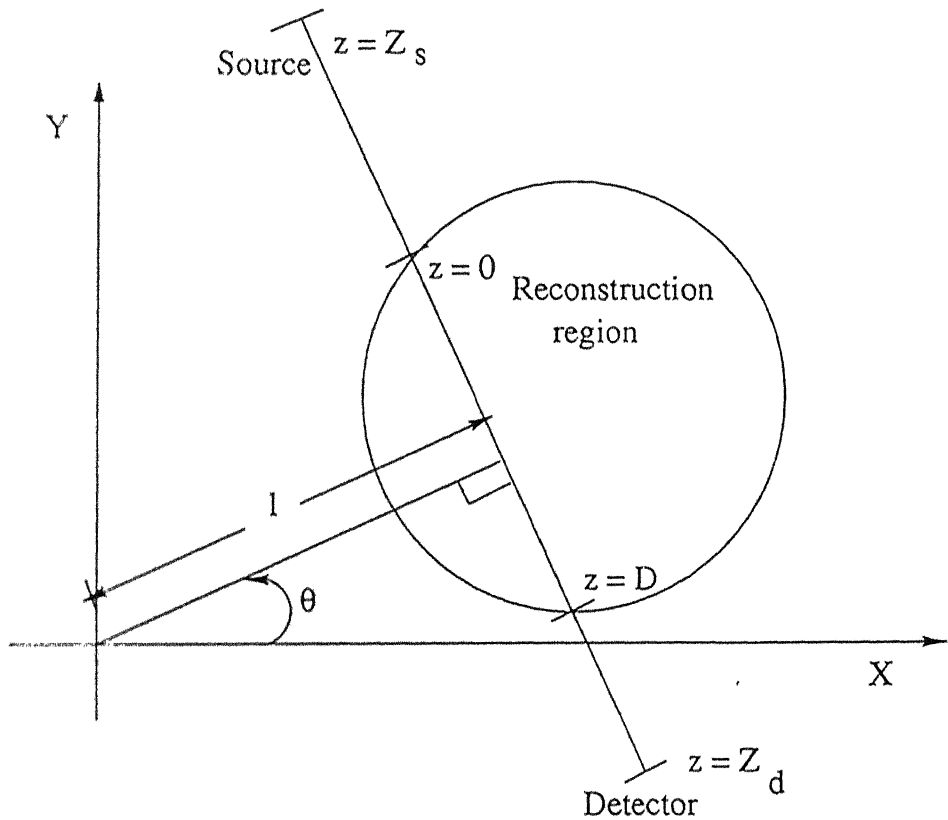


Fig. 2.2 Derivation of polychromatic ray sum.

Theoretical formulation

Let $p_e(z)$ is the probability that a photon of energy e which leaves the source in the direction of the detector will get as far as the point Z without being removed from the beam. Let $q_e(z, \Delta z)$ is the probability that a photon of energy e , which already traveled up to Z from source is removed before it gets to a distance $Z+\Delta Z$ from the source. Then we can write

$$\begin{aligned} p_e(z + \Delta z) &= p_e(z) [1 - q_e(z, \Delta z)] \\ &= p_e(z) - p_e(z) q_e(z, \Delta z). \end{aligned} \quad (2.14)$$

We can write $\mu_e(z)$ as

$$\mu_e(z) = \lim_{\Delta z \rightarrow 0} \frac{q_e(z, \Delta z)}{\Delta z}. \quad (2.15)$$

From Eq. 2.14

$$\frac{p_e(z + \Delta z) - p_e(z)}{\Delta z} \cdot \frac{1}{p_e(z)} = - \frac{q_e(z, \Delta z)}{\Delta z}. \quad (2.16)$$

Taking $\Delta z \rightarrow 0$, we get

$$\frac{p'_e(z)}{p_e(z)} = - \lim_{\Delta z \rightarrow 0} \frac{q_e(z, \Delta z)}{\Delta z}. \quad (2.17)$$

From Eqs. 2.15 and 2.17

$$\frac{p'_e(z)}{p_e(z)} = - \mu_e(z). \quad (2.19)$$

Integration of both sides from Z_s to Z_d leads to

$$\ln p_e(z_d) - \ln p_e(z_s) = - \int_{z_s}^{z_d} \mu_e(z) dz. \quad (2.20)$$

Recalling the definition of $p_e(z)$, $p_e(z_s) = 1$ (hence $\ln p_e(z_s) = 0$), and so

Theoretical formulation

$$\ln p_e(z_d) = - \int_{z_s}^{z_d} \mu_e(z) dz . \quad (2.21)$$

$$p_e(z_d) = \exp \left[- \int_{z_s}^{z_d} \mu_e(z) dz \right] . \quad (2.22)$$

Suppose that S_e photons of energy e leave the source in the direction of the detector, and that δ_e is the efficiency of the detector at energy e . Then, on an average, the number of photons of energy e counted by the detector is

$$\begin{aligned} A_p &= S_e \delta_e p_e(z_d) \\ &= S_e \delta_e \exp \left[- \int_0^D \mu_e(z) dz \right] \\ &= S_e \delta_e k_e \exp \left[- \int_0^D \mu_e(z) dz \right] \end{aligned} \quad (2.23)$$

where

$$k_e = \exp \left[- \int_{z_s}^0 \mu_e(z) dz \right] \exp \left[- \int_D^{z_d} \mu_e(z) dz \right] . \quad (2.24)$$

By the Eq. 2.24 the number of photons at energy e counted by the detector during the calibration measurement is

$$\sigma_e = S_e \delta_e k_e \exp \left[- \int_0^D \mu_e^a(z) dz \right] . \quad (2.25)$$

Where μ_e^a is the linear attenuation coefficient of the reference material. Let C_p is the total number of photons detected during the calibration measurement, then the detected spectrum is

$$\tau_e = \frac{\sigma_e}{C_p} . \quad (2.26)$$

Hence polychromatic ray sum is

Theoretical formulation

$$\begin{aligned}
 p &= -\ln\left(\frac{A_p}{C_p}\right) \\
 &= -\ln\left\{\frac{\int_0^E S_e \delta_e k_e \exp\left[-\int_0^D \mu_e(z) dz\right] de}{C_p}\right\} \\
 &= -\ln\left\{\frac{\int_0^E \sigma_e \exp\left[-\int_0^D (\mu_e(z) - \mu_e^a(z)) dz\right] de}{C_p}\right\} \\
 &= -\ln\left\{\int_0^E \tau_e(z) \exp\left[-\int_0^D (\mu_e(z) - \mu_e^a(z)) dz\right] de\right\}
 \end{aligned} \tag{2.27}$$

If reference material is air then $\mu_e^a = 0$.

2.5 Displaying of an image

For displaying of an image the program written by Farhan (1999) is used. For the purpose of displaying the image, the CT numbers are read from the CBP output file and appropriate grey levels assigned corresponding to it. Thus by generating pixels for each of the projection data at their position the CT image can be graphically displayed. The color code is printed adjacent to it for a quick reference.

The color code is a must to extract information from the colored images produced in the present work. The natural choice for the color code was our own solar spectrum “VIBGYOR” in the scale of 0 to 255. Number 0 is represented by ‘Violet’ and 255 by ‘Red’ and the intermediate colors linearly interpolated to represent other numbers.

2.5.1 VIBGYOR Representation of CT Images

The colours in the image are assigned in a manner such that each distinct value in the reconstructed matrix is displayed in a distinct colour. The colour of the pixel is determined by creating a linear scale such that the smallest number in the matrix gets the colour violet and the largest number gets the colour red. The intermediate colours are generated by linearly interpolating between the RGB (Red, Green, and Blue) values of the colours of a rainbow (VIBGYOR: Violet, Indigo, Blue, Green, Yellow, Orange, and Red). The program is written with the OpenGL library in UNIX platform. Reconstruction of tomographic data results in a matrix in which each element corresponds to the magnitude, of the material property being observed, at that point. If we are able to view this matrix in the form of a coloured image, each colour in the image will correspond to the different observed values of the material property, thus providing us with a view to the interior of the object under observation. The VIBGYOR pattern provides a good mode of visualizing the variation in the material properties of the object. This visualization had been extremely simple if we had a fixed number of values for the observable material property and if we had a unique identifier for each colour in a VIBGYOR spectrum. Thus the problem can be broken up into two pieces:

1. Identifying the RGB values for each of the colours required along the VIBGYOR spectrum.
2. Assigning the elements of the matrix to one of these colours based on a linear scaling of all the values in the matrix.

It is a common practice to represent a colour, as a set of three numbers, which correspond to the intensities of Red, Green and Blue, respectively, that when mixed would produce the colour. To tackle the first sub-problem, we took the RGB values of the seven main colours of the rainbow as:

- Violet : 148, 0, 211

Theoretical formulation

- Indigo : 75, 0, 130
- Blue : 0, 0, 255
- Green : 0, 255, 0
- Yellow: 255, 255, 0
- Orange: 255, 165, 0
- Red : 255, 0, 0

In each case 0 corresponds to the minimum possible intensity and 255 corresponds to the maximum possible intensity of the colour (Red, Green or Blue). The program prompts the user to enter the number of colours desired along the VIBGYOR spectrum. Keeping the values of the major colours as given above, the other values are computed by linearly interpolating the Red, Green and Blue components between these major colours. If 20 colours are required to lie between Blue and Green, then the Red component of all these colours is assigned a value of zero. The Green component is calculated as $Green_i = 0 + ((255 - 0) \times i / 20)$, and similarly the Blue component of these colours is calculated as $Blue_i = 255 + ((0 - 255) \times i / 20)$.

The second sub-problem is also tackled by using linear interpolation. The minimum and maximum values occurring in the matrix are determined first. If the number of colours required by the user is n , then $n-2$ values lying evenly spaced between the two limiting values are computed. Now we have n values corresponding to each of the n required colours. While displaying the image the colour to be assigned to each pixel is determined by comparison with these n values. This can be better understood with the following example. Suppose the user asks for a 256 colour long VIBGYOR spectrum, let the smallest value found in the matrix be V_{min} and the largest value is V_{max} . An array of 256 numbers is created and V_{min} and V_{max} are placed in its first and last place, respectively. These and the other 254 values can be computed using the formula:

$$V_i = V_{min} + (V_{max} - V_{min}) \times i / 255 \quad 0 < i < 255.$$

Chapter 3

Simulation of beam hardening effect

In this chapter simulation procedure of beam hardening effect is described for assumed cross sections with the help of chosen X-ray spectra.

3.1 Simulation of polyenergetic projection data

The formula used for simulation of polyenergetic projection data is derived (Eq. 2.28) in chapter 2. It is assumed that the spectrum of the X-ray beam can be approximated by a discrete spectrum consisting of J energies $e(1), e(2), \dots, e(J)$ and that $\tau_{e(J)}$ is the probability that a detected photon (of the X-ray beam through air between the source and the detector) is at energy $e(J)$. Here it is assumed that air is the only reference medium so, that $\mu_e^a = 0$ and the equation become simpler. Let us divide the cross section into I pixels. We will try to estimate the linear attenuation coefficient in each of the I pixels. From the equations 2.12 and 2.27 of the chapter 2 we have

Simulation of beam hardening effect

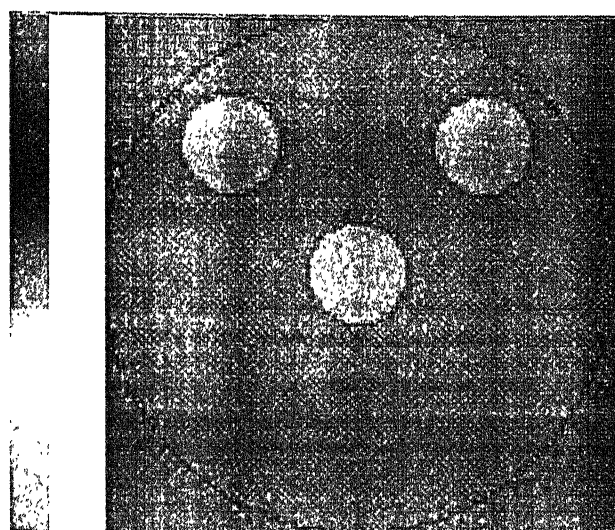
$$m = \sum_{i=1}^I \mu_e^i Z^i \quad (3.1)$$

$$p = -\ln \sum_{j=1}^J \tau_{e(j)} \exp \left[- \sum_{i=1}^I \mu_{e(j)}^i Z^i \right] \quad (3.2)$$

where Z^i denote the length of intersection with the i th pixel of the line from the center of the source to the center of the detector and $\mu_{e(j)}$ is the linear attenuation coefficient at energy e in the i th pixel. Simulation is done on three different types of cross sections. First specimen (S1) is a cross section consisting of three small circles maintained at the same density at each of the energies. For this specimen the X-ray spectrum is taken from Herman(1979).

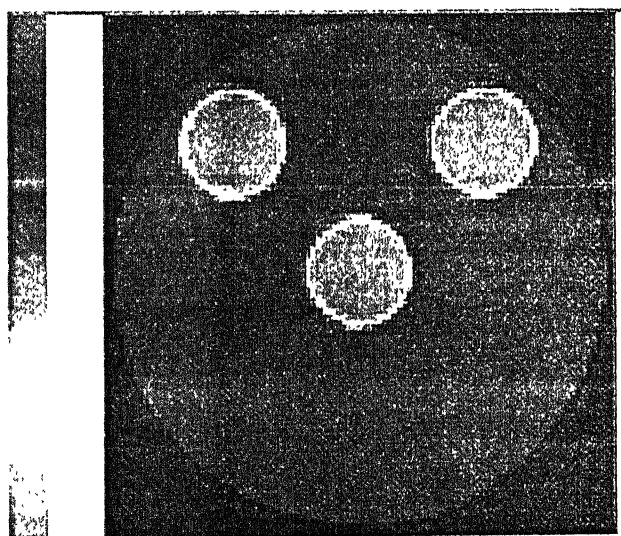
j	$\tau_{e(j)}$	circles μ (in cm^{-1})	non circles μ (in cm^{-1})	Energy (keV)
1	0.1	0.999	0.265	41
2	0.4	0.595	0.226	52
3	0.3	0.416	0.210	60
4	0.2	0.208	0.174	100

Table 3.1 X-ray spectrum for S1.



Min = 0.0000 Max = 0.4160
LAvg = 0.2512 AAvg = 0.2404
File : , NRay : 100, NView : 100

Fig. 3.1 Original image of S1 at energy 60 keV.



Min = 0.0579 Max = 0.4961
LAvg = 0.2666 AAvg = 0.2545
File : , NRay : 100, NView : 100

Fig. 3.2 Beam hardening reconstructed image of S1.

Simulation of beam hardening effect

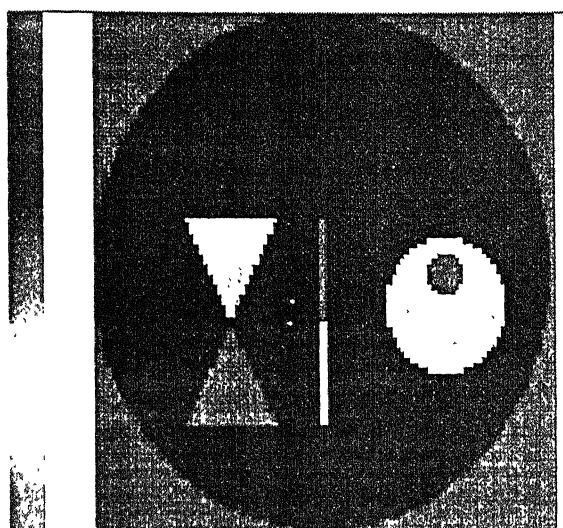
In original image (Fig. 3.1) $\mu = 0.210$ is represented as green colour and $\mu = 0.416$ is represented as red colour. After beam hardening effect (Fig. 3.2) maximum μ found out to be 0.4961. The images are normalized between minimum 0 and maximum 0.4961.

The second specimen (S2) is a cross section consisting of two circles, two triangles, two rectangles. The materials inside them are iron, titanium and void. The spectrum is taken from a NIST (National Institute of Standards and Technologies) Hubbell(1982). The density of void is taken as zero at all the energies.

j	$\tau_{\text{e}(j)}$	Iron μ (in cm^{-1})	Titanium μ (in cm^{-1})	Energy ($1 \cdot 10^{-1} \text{MeV}$)
1	0.3	2.926	1.235	1
2	0.4	1.1496	0.596	2
3	0.3	0.8653	0.473	3

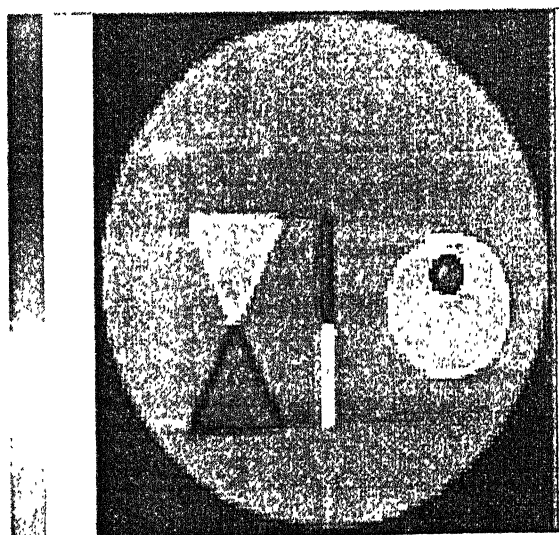
Table 3.2 X-ray spectrum for S2.

Fig. 3.3 is original image of S2 in which titanium is shown in blue colour ($\mu = 0.473$), iron is in yellow colour ($\mu = 0.8653$) and void is in violet colour. After the introduction of the beam hardening effect the maximum pixel value becomes 1.3191. The images are normalized between minimum 0 and maximum 1.3191.



Min = 0.0000 Max = 0.8653
LAvg = 0.5199 AAvg = 0.4962
File : , NRay : 100, NView : 100

Fig. 3.3 Original image of S2 at energy 0.3 MeV.



Min = 0.0201 Max = 1.3191
LAvg = 0.7463 AAvg = 0.7099
File : , NRay : 100, NView : 100

Fig. 3.4 Beam hardening reconstructed image of S2.

Simulation of beam hardening effect

Third specimen (S3) is a star type of object whose μ values at different energies are shown in Table 3.3 which is taken from Herman (1979). There are eight small circles representing the void whose μ values are taken as zero at all the energies.

j	$\tau_{c(j)}$	star μ (in cm^{-1})	non star area μ (in cm^{-1})	Energy (keV)
1	0.4	0.999	0.265	41
2	0.3	0.595	0.226	52
3	0.1	0.416	0.210	60
4	0.1	0.265	0.183	84
5	0.1	0.208	0.174	100

Table 3.3 X- ray spectrum for S3.

In the original image (Fig. 3.5) the maximum pixel value is 0.416. After the beam hardening effect (Fig. 3.6) the maximum pixel value changed to 0.6775. The linear attenuation coefficients of voids are also changed. The images are normalized between minimum 0 and maximum 0.6775.

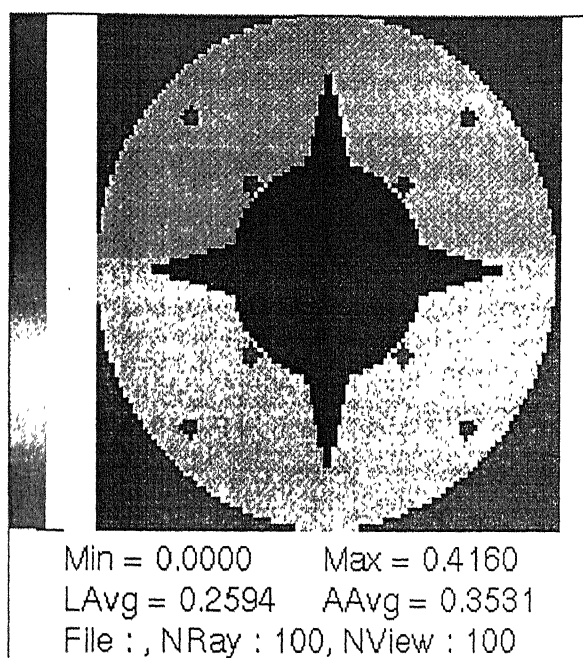


Fig. 3.5 Original image of S3 at energy 60 keV.

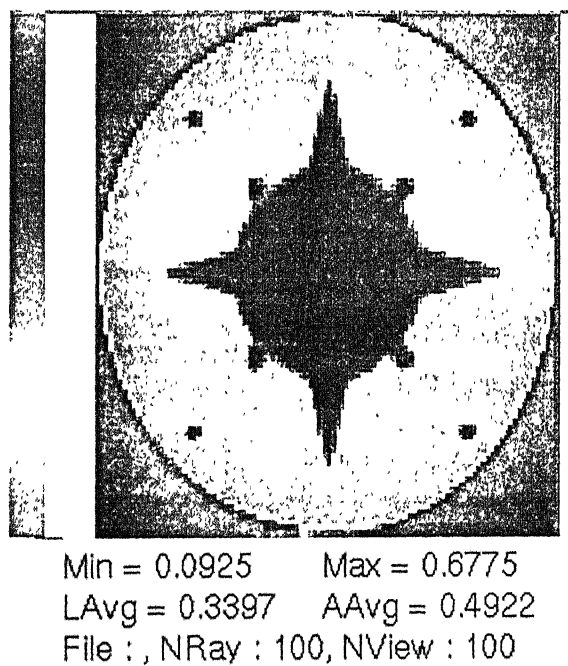


Fig. 3.6 Beam hardening reconstructed image of S3.

Chapter 4

Correction of beam hardening effect

4.1 Correction method for beam hardening

In this chapter the correction procedure is summarized. For correcting the beam hardening effect the procedure adopted by Herman (1979) with few a modifications is used.

For a fixed source and detector position, let m denote the monochromatic ray sum (the measured integral of the linear attenuation coefficient between source and detector if we had an X-ray source that produces only X-rays at energy \bar{e}) and let p denote the polychromatic ray sum (estimate of the integral of the linear attenuation

Correction of beam hardening effect

coefficient between the source and the detector based on measurements with actual polychromatic X-ray source). Using our earlier notation m and p can be defined by

$$m = \int_L \mu(x, y, e) dl \quad (4.1)$$

$$p = -\ln \int_0^E \tau(e) \exp\left(-\int_L \mu(x, y, e) dl\right) de. \quad (4.2)$$

Here E is the highest energy level present in the beam, and $\tau(e)$ is the probability that a detected photon (of the X-ray beam through air between source and detector) is at energy e .

The least expensive type of beam hardening correction can be done by using a function f , which is such that, for each source/detector pair, $f(p)$ is a reasonable estimate of m . Let us refer to the reconstruction from the so corrected polychromatic data $\{f(p)\}$ as the first reconstruction. It is a set of I number, μ'_e , representing the estimated linear attenuation coefficient at energy \bar{e} of the material in the i th of a total of I pixels.

It is assumed that the spectrum of the X-ray can be approximated by a discrete spectrum consisting of J energies $e(1), e(2) \dots e(J)$ and that $\tau_{e(j)}$ is the probability that a detected photon is at energy $e(j)$. We further assume that there are functions g_1, g_2, \dots, g_J such that, for $1 \leq i \leq I$, $g_j(\mu'_e)$ is a reasonably good estimate of the linear attenuation coefficient at energy $e(j)$ of the material in the i th pixel. We describe one such set of functions below. We use $\mu'_{e(j)}$ to denote $g_j(\mu'_e)$. For a fixed source detector pair, let Z' denote the length of intersection with the i th pixel of the line from the center of the source to the center of the detector. We define monochromatic pseudo ray sum \bar{m} , and polychromatic pseudo ray sum \bar{p} by

$$\bar{m} = \sum_{i=1}^I \mu_{e'}^i Z^i. \quad (4.3)$$

$$\bar{p} = -\ln \sum_{j=1}^J \tau_{e(j)} \exp \left[- \sum_{i=1}^I \mu_{e(j)}^i Z^i \right]. \quad (4.4)$$

We see that \bar{m} approximates to m , and \bar{p} approximates to p , and hence $f(\bar{p})$ approximates to $f(p)$. Furthermore, since the line integrals in Eqs. 4.1 and 4.2 are approximated in the same way in Eqs. 4.3 and 4.4, it appears likely that the errors $\bar{m} - m$ and $f(\bar{p}) - f(p)$ in these approximations will be similar (i.e., the difference between these errors will be considerably smaller than either of the errors). Hence $\bar{m} - f(\bar{p}) + f(p)$ is an approximation to m is superior to the use of just $f(p)$. This is true in the sense that

$$\Delta(\{f(p) + \bar{m} - f(\bar{p})\}, \{m\}) < \Delta(\{f(p)\}, \{m\}) \quad (4.5)$$

where Δ represents the root mean square error. The second reconstruction is one obtained from the data $\bar{m} - f(\bar{p}) + f(p)$. Since the second reconstruction is presumably more accurate than the first one, this process can be repeated

The correction procedure followed in the present work is shown Fig. 4.1. For polynomial curve fitting Matlab is used. Matlab solves the system of linear equations in order to obtain the coefficients of the polynomial. The projection data \bar{p} , is a matrix comprising of rows representing number of views and columns representing number of rays. The curve-fitting formula relating \bar{p} and \bar{m} is

$$[\bar{m}] = c_0 + c_1[\bar{p}] + c_2[\bar{p}]^2 + \dots + c_n[\bar{p}]^n \quad (4.6)$$

Where the coefficients c_i 's are found by the generalized vandermonde matrix method.

Correction of beam hardening effect

For the simple case

$$y = c_0 + c_1x + c_2x^2 + \dots + c_nx^n \quad (4.7)$$

this method reduces to solving the system of linear equations as

$$\begin{bmatrix} 1 & x_0 & x_0^2 & . & . & . & x_0^n \\ 1 & x_1 & x_1^2 & . & . & . & x_1^n \\ . & . & . & . & . & . & . \\ . & . & . & . & . & . & . \\ . & . & . & . & . & . & . \\ 1 & x_n & x_n^2 & . & . & . & x_n^n \end{bmatrix} \begin{bmatrix} c_0 \\ c_1 \\ . \\ . \\ . \\ c_n \end{bmatrix} = \begin{bmatrix} y_0 \\ y_1 \\ . \\ . \\ . \\ y_n \end{bmatrix} \quad (4.8)$$

For regression analysis using matrices, this is expanded into a matroid equation.

For the specimen S1 the initial guess is taken as cross section consisting of two circles. For the specimen S2 the initial guess is taken as cross section consisting of one triangle and one circle. For the specimen S3 the initial guess is taken as cross section consisting of single circle at the center.

Correction of beam hardening effect

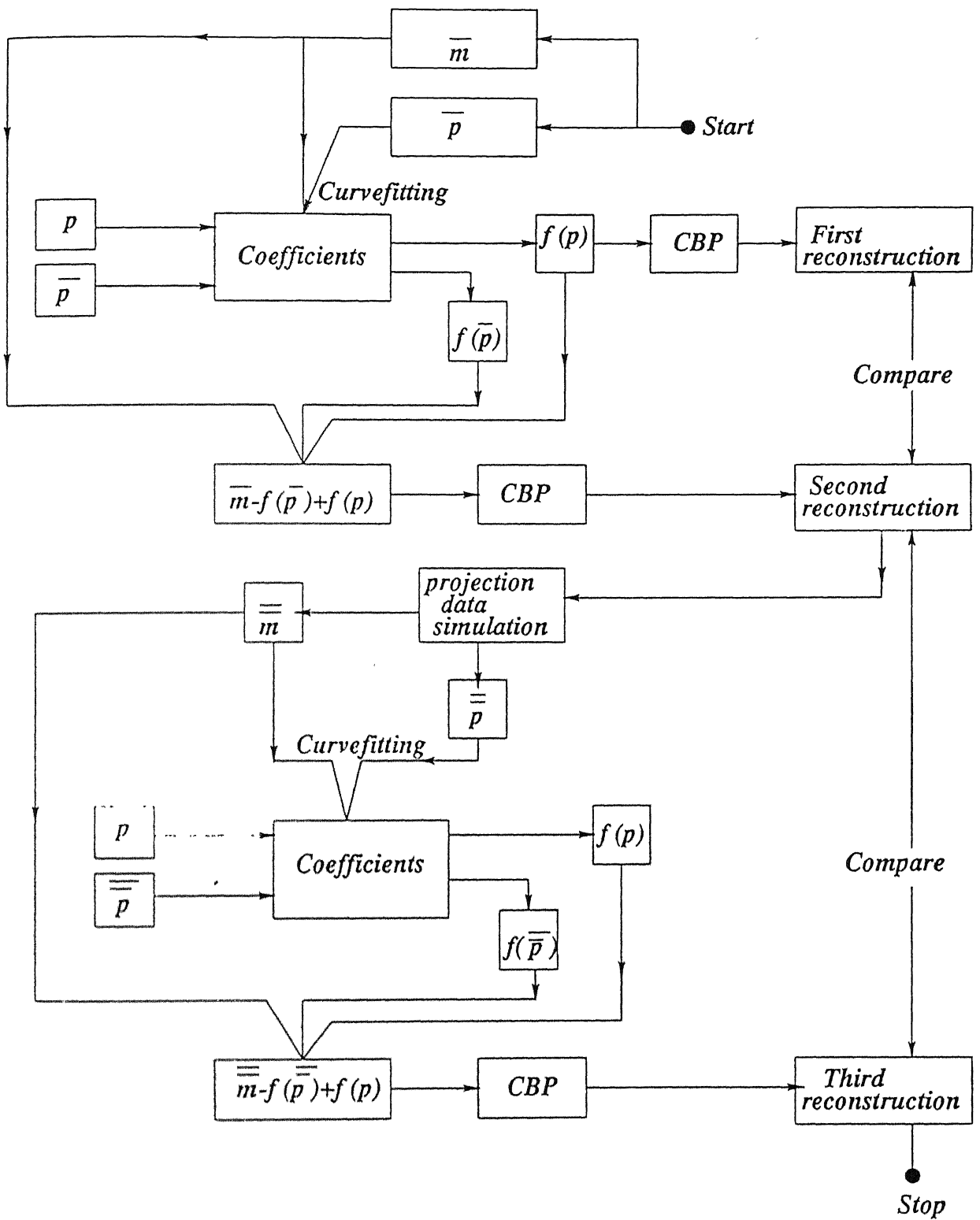
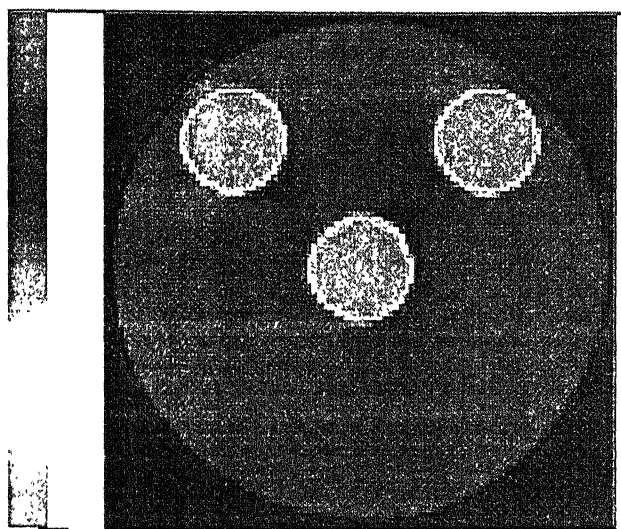
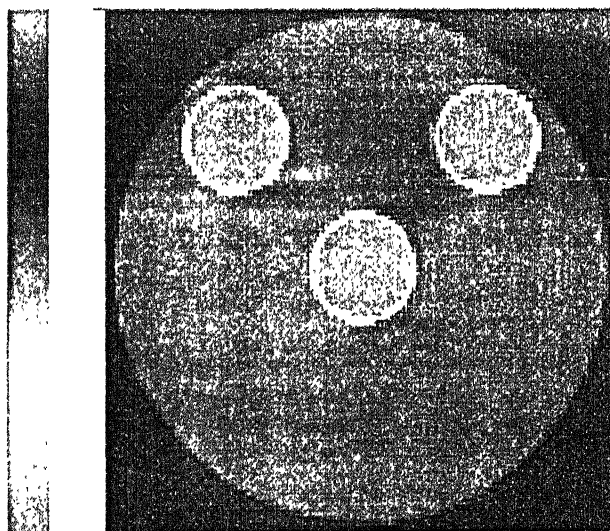


Fig. 4.1 Flow chart representing the correction procedure.



Min = 0.0473 Max = 0.4641
LAvg = 0.2485 AAvg = 0.2413
File : , NRay : 100, NView : 100

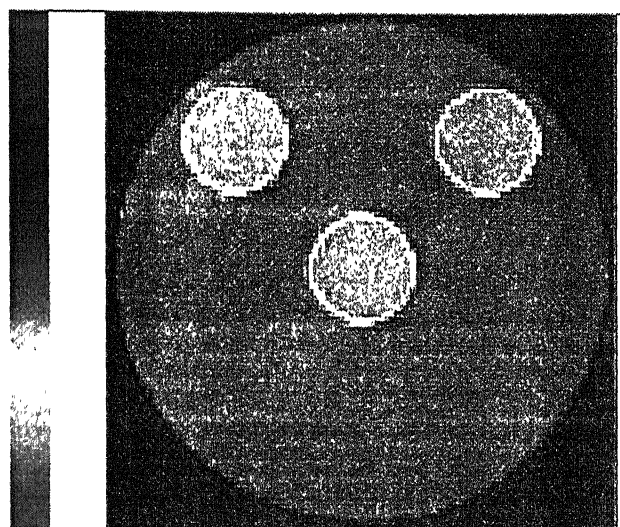
Fig. 4.2 First reconstructed image of S1 at energy 60 keV.



Min = 0.0569 Max = 0.4392
LAvg = 0.2535 AAvg = 0.2415
File : , NRay : 100, NView : 100

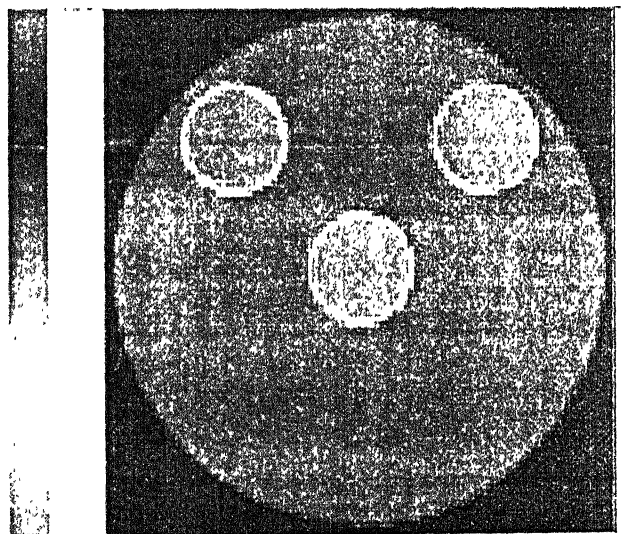
Fig. 4.3 Second reconstructed image of S1 at energy 60 keV.

Correction of beam hardening effect



Min = 0.0437 Max = 0.4442
LAvg = 0.2540 AAvg = 0.2434
File : . NRay : 100. NView : 100

Fig. 4.4 Third reconstructed image of S1 at energy 60 keV.



Min = 0.0561 Max = 0.4229
LAvg = 0.2494 AAvg = 0.2406
File : , NRay : 100, NView : 100

Fig.4.5 Monochromatic reconstructed image of S1 at energy 60 keV.

Correction of beam hardening effect

Fig. 4.2 is the first reconstructed image of S1 obtained from the projection data $f(p)$ in which third circle appears light. The area outside the circles, which is green in the original image (Fig. 3.1) appears very light. The second reconstructed image (Fig.4.3) is obtained from the data $\bar{m} - f(\bar{p}) + f(p)$ in which all the three circles appear clearly. The third reconstructed image (Fig. 4.4) is obtained from the projection data $\bar{\bar{m}} - f(\bar{\bar{p}}) + f(p)$, it matches well with the monochromatic reconstructed image (Fig. 4.5). The maximum pixel value in the beam hardening reconstructed image (Fig. 3.2) is 0.4961, which becomes 0.4442 after the third reconstruction (Fig. 4.4).

Correction of beam hardening effect

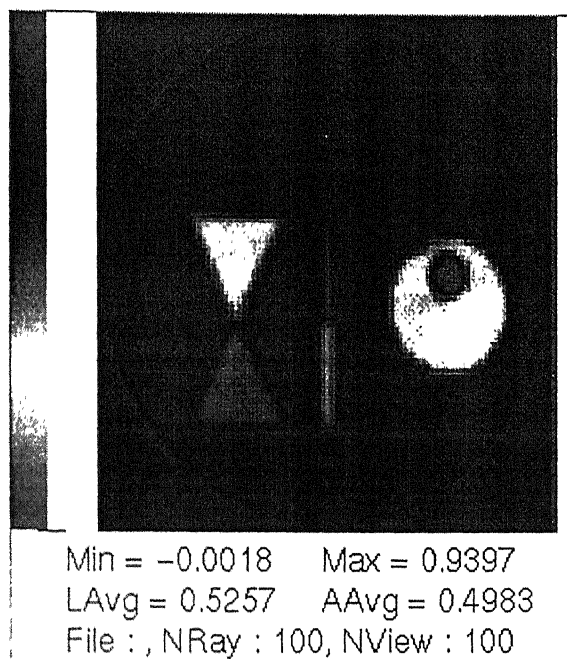


Fig. 4.6 First reconstructed image of S2 at energy 0.3 MeV.

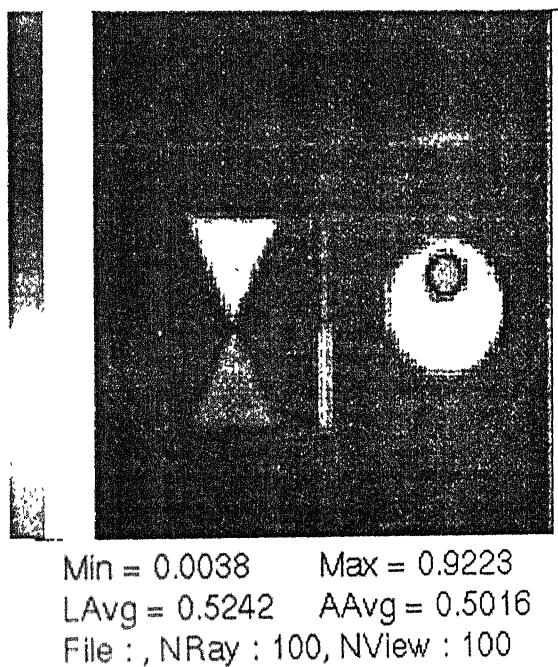


Fig. 4.7 Third reconstructed image of S2 at energy 0.3 MeV.

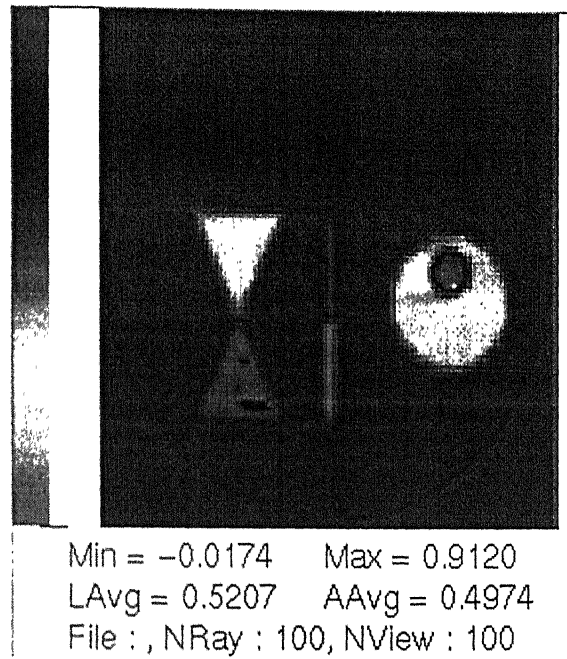
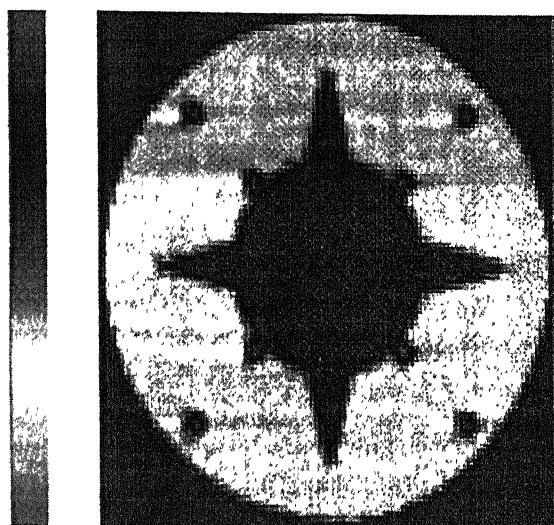


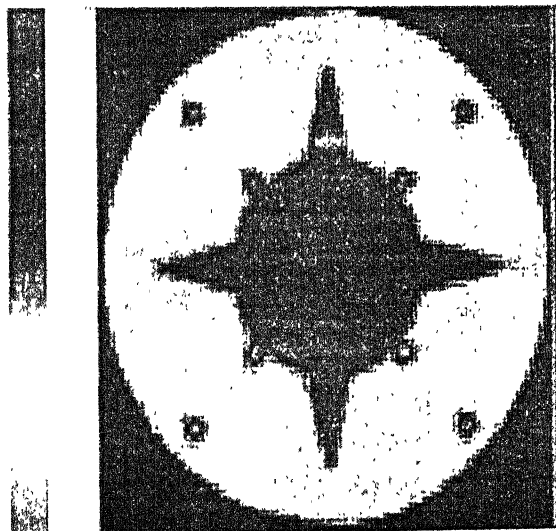
Fig. 4.8 Monochromatic reconstructed image of S2 at energy 0.3 MeV.

Fig. 4.6 is the first reconstructed image of S2 obtained from the projection data $f(p)$. Third reconstructed image (Fig. 4.7) is obtained from the projection data $m - f(p) + f(p)$, which is matching well with the monochromatic reconstructed image (Fig. 4.8). The maximum pixel value in the beam hardening reconstructed image (Fig. 3.4) is 1.3191, which becomes 0.9223 after third reconstruction (Fig. 4.7).



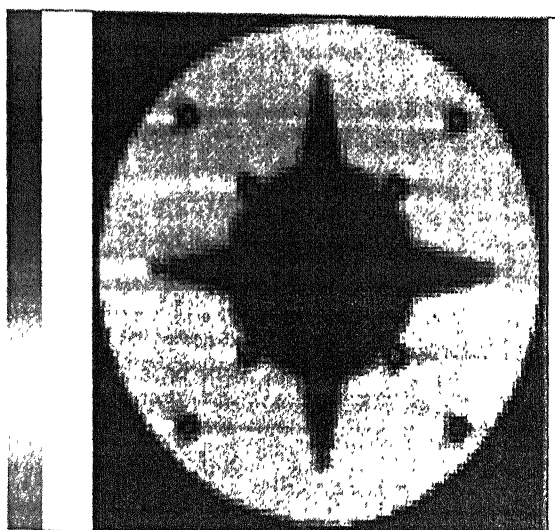
Min = 0.0377 Max = 0.4661
LAvg = 0.2310 AAvg = 0.3485
File : , NRay : 100, NView : 100

Fig. 4.9 First reconstructed image of S3 at energy 60 keV.



Min = 0.0312 Max = 0.4598
LAvg = 0.2408 AAvg = 0.3484
File : , NRay : 100, NView : 100

Fig. 4.10 Second reconstructed image of S3 at energy 60 keV.



Min = 0.0428 Max = 0.4549
LAvg = 0.2655 AAvg = 0.3556
File : , NRay : 100, NView : 100

Fig. 4.11 Monochromatic reconstructed image of S3 at energy 60 keV.

Fig. 4.9 is the first reconstructed image of S3 obtained from the projection data $f(p)$ in which the star appears dark blue. The second reconstructed image (Fig.4.10) is obtained from the data $m - f(p) + f(p)$ in which star area appears as light blue colour. Second reconstructed image (Fig. 4.10) is matching well with the monochromatic reconstructed image (Fig. 4.11). The maximum pixel value in the beam hardening reconstructed image (Fig. 3.6) is 0.6775, which becomes 0.4598 after the second reconstruction (Fig. 4.10).

Chapter 5

Results and Discussion

5.1 Error measurements

Average pixel errors and root mean square errors are calculated for projection data as well as the reconstruction data for all the three specimens. Tables 5.1 to 5.4 give the error estimates for S1. Tables 5.5 to 5.8 give the error estimates for S2. Tables 5.9 to 5.12 give the error estimates for S3. Results are quite encouraging. Error values are decreasing after each iteration.

Results and Discussions

Energy (in keV)	$ m - p $	$ m - f(p) $	$ m - [\bar{m} - f(\bar{p}) + f(p)] $
100	0.1073	0.0150	0.0035
60	0.0190	0.0050	0.0011
52	0.0364	0.0065	0.0016
41	0.1656	0.0317	0.0077

Table S.1 Average pixel errors between the projection data for S1.

Energy (in keV)	$ m - p $	$ m - f(p) $	$ m - [\bar{m} - f(\bar{p}) + f(p)] $
100	0.1242	0.0206	0.0086
60	0.0243	0.0070	0.0029
52	0.0439	0.0086	0.0038
41	0.2013	0.0430	0.0182

Table S.2 Root mean square errors between the projection data for S1.

Results and Discussions

Energy (in keV)	Beam hardening	Monochromatic	After applying Correction
100	0.8026	0.0247	0.0276
60	0.0411	0.0340	0.0345
52	0.0514	0.0405	0.0411
41	0.1150	0.0558	0.0593

Table S.3 Average pixel errors between the original and various reconstructed data for S1.

Energy (in keV)	Beam hardening	Monochromatic	After applying Correction
100	0.1772	0.0462	0.0471
60	0.0645	0.0600	0.0599
52	0.0760	0.0703	0.0705
41	0.1823	0.0977	0.1009

Table S.4 Root mean square errors between the original and various reconstructed data for S1

Energy (in MeV)	$ m - p $	$ m - f(p) $	$ m - [\bar{m} - f(\bar{p}) + f(p)] $
0.1	0.9908	0.0440	0.0121
0.2	0.1307	0.0021	0.0007
0.3	0.3383	0.0057	0.0017

Table 5.5 Average pixel errors between the projection data for S2.

Energy (in MeV)	$ m - p $	$ m - f(p) $	$ m - [\bar{m} - f(\bar{p}) + f(p)] $
0.1	1.0711	0.0555	0.0246
0.2	0.1336	0.0031	0.0015
0.3	0.3527	0.0076	0.0035

Table 5.6 Root mean square errors between the projection data for S2.

Results and Discussions

Energy (in MeV)	Beam hardening	Monochromatic	After applying Correction
0.1	0.6048	0.2222	0.2244
0.2	0.1581	0.1008	0.1009
0.3	0.2477	0.0789	0.0792

Table 5.7 Average pixel errors between the original and various reconstructed data for S2.

Energy (in MeV)	Beam hardening	Monochromatic	After applying Correction
0.1	0.6970	0.3714	0.3721
0.2	0.2050	0.1705	0.1706
0.3	0.2658	0.1340	0.1342

Table 5.8 Root mean square errors between the original and various reconstructed data for S2.

Results and Discussions

Energy (in keV)	$ m - p $	$ m - f(p) $	$ m - [\bar{m} - f(\bar{p}) + f(p)] $
100	0.4945	0.0277	0.0175
84	0.4235	0.0236	0.0150
60	0.2343	0.0138	0.0091
52	0.0157	0.0027	0.0017
41	0.4787	0.0391	0.0238

Table 5.9 Average pixel errors between the projection data for S3.

Energy (in keV)	$ m - p $	$ m - f(p) $	$ m - [\bar{m} - f(\bar{p}) + f(p)] $
100	0.5082	0.0379	0.0257
84	0.4350	0.0324	0.0220
60	0.2399	0.0193	0.0134
52	0.0178	0.0033	0.0028
41	0.4971	0.0521	0.0346

Table 5.10 Root mean square errors between the projection data for S3.

Results and Discussions

Energy (in keV)	Beam hardening	Monochromatic	After applying Correction
100	0.3091	0.0309	0.0383
84	0.2735	0.0399	0.0452
60	0.1834	0.0637	0.0645
52	0.1003	0.0923	0.0930
41	0.3301	0.1569	0.1681

Table 5.11 Average pixel errors between the original and various reconstructed data for S3.

Energy (in keV)	Beam hardening	Monochromatic	After applying Correction
100	0.3314	0.0553	0.0581
84	0.2936	0.0702	0.0706
60	0.2063	0.1101	0.1089
52	0.1638	0.1577	0.1585
41	0.3650	0.2656	0.2756

Table 5.12 Root mean square errors between the original and various reconstructed data for S3.

5.2 Simulation results

Due to the beam hardening effect it may be possible that the cross section under consideration may be subject to change. But such situation is did not occur in any of the three specimens simulated.

Present simulation results also show that second and third order polynomials are sufficient for correcting the beam hardening effects. After applying the correction the reconstruction results shows that they are not much dependent on the initial guess.

As for as the choice of the energy of the reconstruction is considered, from the error estimates and reconstructed images it is observed, that most of the times the energy for which the root mean square error between the polychromatic and monochromatic projection data is least, gives the best results. The observed results shows that 2 to 3 reconstructions are enough for correcting the beam hardening effect, because no significant improvement in the reconstruction was subsequently found.

Chapter 6

Conclusions

In all the three tested specimens it is observed that the polychromatic projection data is quantitatively different from the monochromatic projection data, but not qualitatively. More simulation is to be done with different assumed cross sections.

The reconstructed results reported are quite good in view of the error estimates. After applying the correction the polychromatic reconstructed images match well with the monochromatic reconstructed images.

In the present work the number of rays and the number of views are taken as 100 in all the three tested specimens. More simulation has to be done with different number of rays and views in order to see their effect.

References

Herman GT(1980): *Image reconstruction from Projections: The mathematics of Computerized Tomography.* Academic publishers New York.

Herman GT(1979): *Demonstration of Beam Hardening Correction in Computed Tomography of the Head.* J. Computed Assist. Tomography, Vol. 3, 373-378.

Herman GT(1979): *Correction for Beam Hardening in Computed Tomography.* Phys. Med. Biol. 24:81-106.

Herman GT, Trivedi SS (1983): *A Comparative Study of Two Postreconstruction Beam Hardening Correction Methods.* IEEE Trans. Med. Imaging, Vol. MI-2, No. 3.

Hubbell JH(1982): *Photon Mass Attenuation and Energy Absorption Coefficients from 1 keV to 20 MeV.* Int. J. Appl. Radit. Isot. 33, 1269-1290.

Lewitt RM(1983): *Reconstruction Algorithms: Transform Methods.* Proceedings IEEE, Vol. 71, No. 3, 390-408.

Munshi P, Maisal M and Reiter H(1997): *Experimental aspects of the approximate error formulae for tomographic reconstruction.* Materials Evaluation, 55(2), 188-199.

Munshi P, Davis GR and Elliott(1996): *An Analysis of Biological Tissues Using the Tomographic Reconstruction error Formula.* J. X-ray Science and Technology 6, 63-76.

Natterer F(1986): *The Mathematics of Computerized Tomography.* John Wiley and Sons, NewYork.

130922

This book is to be returned on the
date last stamped.

[illegible]

TH
NET/2000/M
K897A
A130922